J Adv Ceram

Research Article

Achieving superior thermal stability in vat photopolymerized silica-based ceramic cores via kyanite-induced expansion compensation

Boran Wang[1], Zhongyan Wang[1], Xin Li[2], Yu Chen[1], Rui Ge[1], Yongkang Yang[3], Jiachen Liu[1], Anran Guo[1,✉]

Cite this article: Wang B, Wang Z, Li X, et al. *J Adv Ceram* 2026, **15**(6): 9221313. https://doi.org/10.26599/JAC.2026.9221313

ABSTRACT: Vat photopolymerization (VPP) three-dimensional (3D) printing has emerged as a predominant technology for fabricating complex-shaped ceramic cores used in aeroengine hollow turbine blades. However, the inherent limitations of VPP 3D printing-fabricated silica-based cores, such as excessive sintering shrinkage and high-temperature deflection, have severely restricted their application in high-performance investment casting. In this study, we proposed a novel strategy to overcome this challenge by introducing kyanite into the silica-based ceramic core. The influence of kyanite content on microstructural evolution and comprehensive properties was systematically explored, and a ceramic core quality index (CQI) model was further established to evaluate the comprehensive performance.

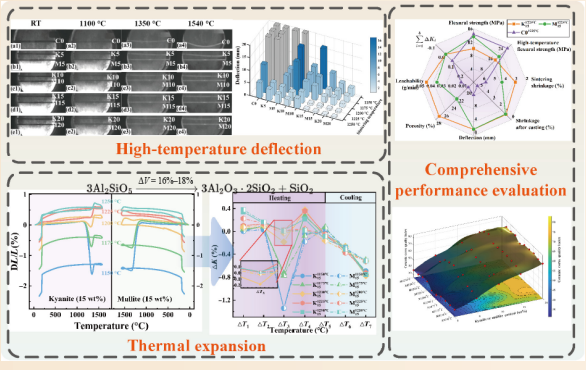

The results indicated that when the kyanite content exceeded 15 wt%, the volume expansion resulting from high-temperature decomposition effectively inhibited sintering shrinkage within the temperature range of 1300–1400 °C. Furthermore, the columnar mullite crystals generated from decomposition acted as the key factor enhancing the high-temperature performance. Optimal comprehensive properties, corresponding to a maximum CQI score of 78.85, were achieved with a kyanite content of 15 wt% and a sintering temperature of 1225 °C. Under this condition, the sintering shrinkage and casting shrinkage of ceramic cores were reduced to 3.06% and 0.86%, respectively. Additionally, the high-temperature deflection was significantly decreased to 0.82 mm, while the flexural strength and high-temperature flexural strength reached 10.06 and 27.05 MPa, respectively. This study provides a novel strategy for fabricating silica-based ceramic cores with lower sintering and casting shrinkage while elucidating the regulatory mechanism of kyanite on the core properties.

KEYWORDS: ceramic cores; vat photopolymerization (VPP); shrinkage compensation; thermal expansion; creep resistance; comprehensive performance evaluation

1 Introduction

With the increasing demand for higher thrust-to-weight ratios in aeroengines, turbine blades must incorporate complex internal cooling structures to withstand operating temperatures that exceed the thermal limits of superalloys [1–3]. To fabricate these intricate internal geometries, ceramic cores are employed as the critical forming elements during investment casting, directly dictating the dimensional precision and performance of the blades [4,5]. The primary function of the ceramic core is to maintain structural stability under high-temperature casting conditions, thereby playing a decisive role in determining the dimensional precision and structural integrity of the internal air-cooling channels within hollow blades [6–8]. However, with the rapid evolution of cooling schemes for hollow turbine blades, the geometries of ceramic cores are becoming increasingly complex. Constrained by the lengthy mold fabrication cycles and high costs, traditional hot injection molding is becoming increasingly inadequate for satisfying the urgent demands for the rapid development of advanced turbine blades [9,10]. Hence, there is an urgent need for an advanced rapid prototyping process capable of producing ceramic cores with intricate structures.

In recent years, vat photopolymerization (VPP) technology has attracted significant interest in the field of ceramic core

[1] School of Materials Science and Engineering, Key Lab of Advanced Ceramics and Machining Technology of Ministry of Education, Tianjin University, Tianjin 300072, China. [2] Science and Technology on Advanced High Temperature Structural Materials Laboratory, Beijing Institute of Aeronautical Materials, Beijing 100095, China. [3] State Key Laboratory of Materials Processing and Die & Mould Technology, School of Materials Science and Engineering, Huazhong University of Science and Technology, Wuhan 430074, China.

✉ Corresponding author. E-mail: arguo@tju.edu.cn

Received: February 10, 2026; Revised: April 30, 2026; Accepted: May 2, 2026

manufacturing [11–14]. This technology utilizes light of a specific wavelength to induce the cross-linking polymerization of photosensitive components within the ceramic slurry, thereby achieving layer-by-layer material stacking [15,16]. Compared with traditional processes, VPP three-dimensional (3D) printing technology effectively overcomes the limitations of mold-based manufacturing [17,18]. This not only significantly shortens the development cycle and reduces the production cost but also enables the fabrication of highly complex and precise structures of ceramic cores through its superior forming precision [18–20]. However, the application of VPP technology to high-performance ceramic cores still faces severe challenges. Since green bodies consist of a high proportion of organic components, obstructed gas escape channels during pyrolysis can induce localized stress concentrations, resulting in pores or microcracks [21,22]. The subsequent high-temperature sintering process densifies the ceramic cores but causes volumetric shrinkage and deformation that reduce dimensional accuracy [23,24]. Finally, during the directional solidification casting process, ceramic cores face the risks of mechanical and thermal shocks, creep rupture, and thermal expansion [25]. If the high-temperature flexural strength, creep resistance, and high-temperature stability of the core cannot adapt to this harsh environment, it will lead to core fracture, deformation, or the formation of ceramic core inclusions, ultimately decreasing the quality of hollow blades [26,27]. Therefore, the high-temperature performance of the VPP 3D printing ceramic core is the key to improving the yield of investment casting. Silica-based ceramic cores currently account for more than 90% of the cores used in the investment casting of superalloy turbine blades, owing to their low coefficient of thermal expansion, excellent thermal shock resistance, favorable sintering performance, high-temperature structural stability, and easy leachability in alkaline solutions [28,29]. However, silica-based ceramic cores undergo significant shrinkage behaviors during the heating process from ambient temperature to above 1500 °C [26]. At approximately 1200 °C, viscous flow-dominated densification induces ceramic core shrinkage and creep deformation [30]. When the temperature increases to 1350 °C, the crystallization of amorphous silica into cristobalite accelerates. However, the precipitation of cristobalite enhances the core's high-temperature strength sufficiently to tolerate creep deformation [31–33]. However, relying solely on the intrinsic crystallization of fused silica is insufficient to meet the high-temperature performance required for single-crystal turbine blade casting. To obtain comprehensive high-temperature performance, extensive research has been conducted to regulate this process by optimizing the material composition and sintering process. Studies indicate that adding silicon carbide [33], fused silica fibers [34], mullite fibers [35], iron oxide [36], or alumina [37,38] to silica-based ceramic cores can promote cristobalite crystallization, significantly enhancing the creep resistance of the ceramic core and inhibiting high-temperature shrinkage. Furthermore, sillimanite group minerals have attracted increasing attention due to their unique high-temperature expansion characteristics, which can be utilized to compensate for sintering shrinkage [39,40]. Among them, the volumetric effect produced by the high-temperature decomposition of kyanite is the most significant, with the decomposition process accompanied by a volume expansion of 16%–18% [41,42]. Research has indicated that kyanite begins to form mullite at 1150 °C and completely transforms into mullite and silica at 1350–1450 °C. Bartlett [43] systematically investigated the decomposition rate, highlighting that this conversion process is highly dependent on both the calcination temperature and the initial grain size of kyanite. Based on this fundamental phase transition, Qin and Pan [44] demonstrated that decomposition-generated mullite forms an interlocking network within the matrix. The expansion effect associated with this transformation increases the porosity of the core and inhibits flow and sintering shrinkage, thereby significantly enhancing the high-temperature creep resistance of the ceramic cores. Recently, Liu *et al.* [20] introduced kyanite into VPP 3D-printed printed silica-based ceramic cores, demonstrating that the decomposition-generated mullite and the associated volume expansion can reduce sintering shrinkage and improve flexural strength. However, volume expansion inevitably induces microcracks, especially since the cristobalite content is high after sintering, which limits the mechanical properties. Moreover, their research primarily focused on a single additive, and a systematic comparative study on the effects of different mullite sources, such as the direct addition of mullite versus decomposition-generated mullite from kyanite, on the properties of 3D-printed ceramic cores is still lacking. Furthermore, the thermal expansion and high-temperature creep resistance of these 3D-printed silica-based ceramic cores have not been comprehensively investigated.

In this work, silica-based ceramic cores were fabricated via VPP 3D printing technology to systematically compare the effects of kyanite and mullite additions. Initially, the study focused on evaluating dimensional changes, specifically probing sintering and casting shrinkage. Subsequently, the high-temperature stability was further analyzed through an investigation of the thermal expansion behavior and high-temperature creep resistance. To quantitatively assess these multidimensional properties, a ceramic core quality index (CQI) evaluation model was established. Through this progressive evaluation, this study aims to achieve synergistic control over the dimensional precision and high-temperature stability of ceramic cores by optimizing the additive content and sintering temperature, thereby providing a robust theoretical basis and technical support for optimizing material formulations for VPP 3D-printed ceramic cores.

2 Experimental

2.1 Raw materials

The ceramic slurry for VPP 3D printing consists of ceramic powders and a photosensitive resin. The ceramic powders used in this study are composed of fused silica, kyanite/mullite, and zirconium silicate. These three powders were supplied by Lianyungang OWA New Materials Technology Co., Ltd., China, and their particle size distributions and morphologies are shown in Fig. 1(b). Trimethylolpropane triacrylate (TMPTA; 1.1 g/cm^3, Shanghai Aladdin Biochemical Science and Technology Co., Ltd., China) and 1,6-hexanediol diacrylate (HDDA; 1.01 g/cm^3, Shanghai Aladdin Biochemical Science and Technology Co., Ltd., China) were employed as functional monomers. Additionally, 2,4,6-trimethylbenzoyldiphenylphosphine oxide (TPO-L; Shanghai Yinchang Co., Ltd., China) served as the photoinitiator, and BYK-111 (BYK LIMITED, Germany) was used as the dispersant.

2.2 Sample preparation

The VPP 3D printing process flow for silica-based ceramic cores is illustrated in Fig. 1. First, HDDA and TMPTA were mixed at a mass ratio of 4 : 1. Then, TPO-L (1 wt% relative to the resin mass) and BYK-111 (2 wt% relative to the ceramic powder mass) were added and thoroughly mixed to prepare the photosensitive resin. Subsequently, the mixed ceramic powders (specific formulations are detailed in Table 1) were incorporated into the prepared photosensitive resin. Finally, the mixture was ball-milled in a planetary ball mill (QM-3SP2, Nanjing University Instrument

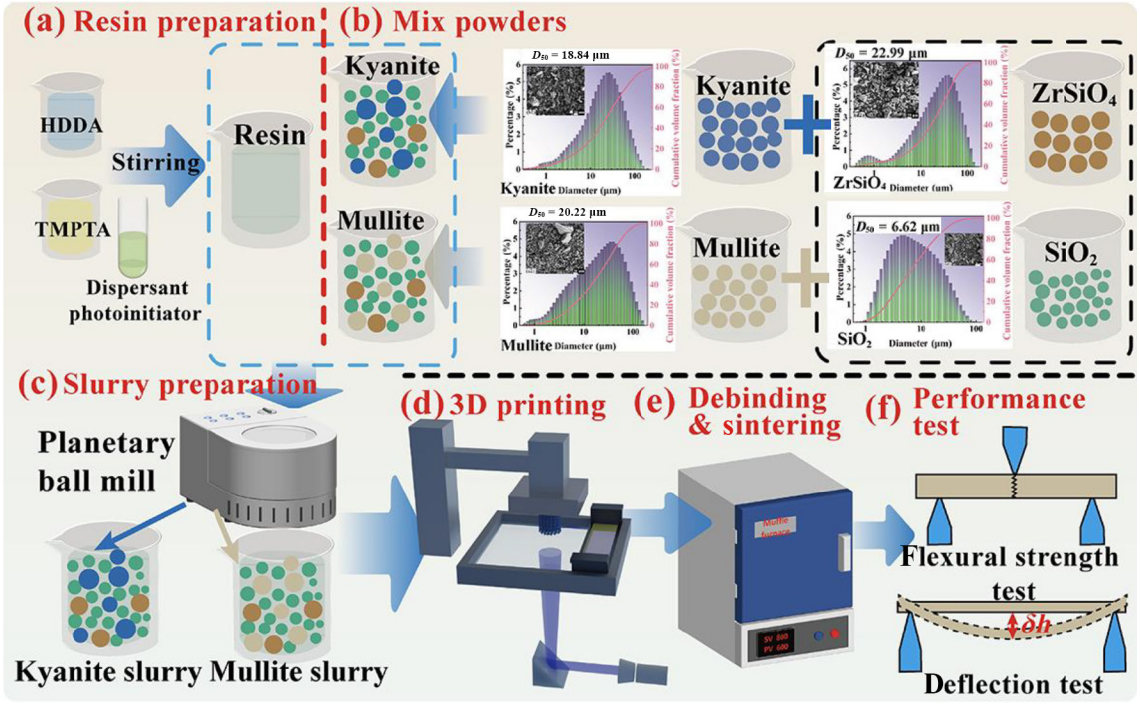

Fig. 1 Schematic diagram of preparation process of ceramic core samples with added kyanite/mullite.

Factory, China) at 200 r/min for 2 h to yield a homogeneous ceramic slurry with a solid loading of 65 vol% (Fig. 1(c)). Rectangular green bodies were fabricated using a 3D printer (AutoCERA-L, Beijing Ten Dimensions Technology Co., Ltd., China) (Fig. 1(d)) with dimensions of 60 mm × 10 mm × 4 mm and 120 mm × 6 mm × 2 mm. After printing, the samples were cleaned by immersion in alcohol to remove the residual uncured slurry and subsequently dried. The debinding and sintering process was conducted in a muffle furnace (KSL-1400x, Hefei Kejing Materials Technology Co., Ltd., China) (Fig. 1(e)). For debinding, the samples were heated to 600 °C at a rate of 0.5 °C/min with a dwell time of 2 h. Subsequently, the temperature was increased at 2 °C/min to the target sintering temperatures (1150, 1175, 1200, 1225, and 1250 °C) and held for 6 h.

2.3 Characterization

According to HB 5353.3-2004, the flexural strength and high-temperature flexural strength were determined via a three-point bending test with a loading speed of 5 mm/min and a span of 30 mm. The flexural strength at room temperature was measured using an electronic universal testing machine (WDW-10, Changchun Kexin Test Instrument Co., Ltd., China), while the high-temperature flexural strength was evaluated at 1540 °C using a high-temperature testing machine (WDW-G100, Jinan Yinuo Century Experimental Co., Ltd., China). High-temperature deflection was analyzed using a double-support thermal deformation method (Fig. 1(f)). Rectangular specimens with dimensions of 120 mm × 6 mm × 2 mm were tested under a support span of 100 mm in accordance with HB 5353.4-2004. They were heated to 1540 °C at a rate of 10 °C/min and held for 1 h. A thermos-optical measuring system (TOMMI plus, Fraunhofer, Germany) with a maximum deflection measurement range of 20 mm was employed to *in situ* monitor the thermal deformation during the heating process. The permanent deformation, defined as the height difference before and after heating, was measured using a vernier caliper and recorded as the high-temperature deflection. The porosity and porosity after casting were tested in accordance with HB 5353.1-2004, and the porosity of the samples was calculated by Eqs. (S1) and (S2) of Note S1 in the Electronic Supplementary Material (ESM). Furthermore, the sintering shrinkage and casting shrinkage were evaluated by referencing HB 5353.2-2004, and the shrinkage of samples was calculated by Eqs. (S3) and (S4) of Note S1 in the ESM. For each testing group, the reported data represent the average of at least five specimens. For thermal expansion measurements, the HB 5353.5-2004 standard was utilized as the primary reference.

Thermal expansion curves (from room temperature to 1580 °C) were measured using a dilatometer (DIL402 Expedis Classic, Netzsch, Germany) under a load of 0.2 N and a heating rate of 10 °C/min with specimens measuring 6 mm × 6 mm × 25 mm. The microstructure of the ceramic cores was examined by field emission scanning electron microscope (FE-SEM; Nova nanoSEM450, FEI, USA). The phase compositions of the ceramic cores, varying in sintering temperatures and kyanite/mullite contents, were identified via an X-ray diffractometer (XRD; D8 Advance, Bruker, Germany). Following the HB 5353.6-2004 standard, the leachability of the samples was evaluated after the

Table 1 Initial formulations of ceramic powder for ceramic cores

No.	Powder weight fraction (wt%)			
	Fused silica	Kyanite	Mullite	$ZrSiO_4$
C0	95	0	0	5
K5	90	5	0	5
K10	85	10	0	5
K15	80	15	0	5
K20	75	20	0	5
M5	90	0	5	5
M10	85	0	10	5
M15	80	0	15	5
M20	75	0	20	5

simulated casting heat treatment, and the leachability of samples was determined by Eq. (S5) of Note S1 in the ESM.

3 Results and discussion

To address critical issues associated with VPP 3D-printed ceramic cores, such as significant sintering shrinkage and insufficient high-temperature stability, this study incorporates kyanite—characterized by its excellent thermal expansion properties—as a modifying additive into silica-based ceramic cores. The objective is to reduce shrinkage during the debinding–sintering process and enhance high-temperature stability. Given that kyanite decomposes to form mullite at elevated temperatures, a mullite-based group was established as a comparative control. By systematically characterizing and analyzing the differences between the two groups in terms of sintering shrinkage behavior, high-temperature stability, and mechanical properties, this study elucidates the modification mechanism of kyanite.

3.1 Phase analysis

The ceramic slurry for VPP 3D printing is primarily composed of a photosensitive resin and ceramic powder. During the debinding and sintering processes, variations in the ceramic powder composition and the sintering temperature directly determine the microstructural evolution and final properties of the ceramic cores. Therefore, the effects of different ceramic powder compositions and sintering temperatures on the phase composition, along with their underlying regulatory mechanisms, require systematic investigation for further clarification.

Figure 2(a) illustrates the scanning electron microscopy (SEM) images of VPP 3D-printed ceramic cores with varying kyanite/mullite additions and sintering temperatures. Additionally, a comprehensive multiscale analysis (Note S2 in the ESM) confirms that kyanite is uniformly distributed within the ceramic cores at different content levels. At a sintering temperature of 1150 °C (Figs. 2(a1)–2(c1)), numerous pores are distributed in the ceramic cores. Upon increasing the sintering temperature to 1250 °C, the interparticle bonding of the C0 sample (Fig. 2(a3)) exhibits significantly enhanced interparticle bonding and greatly improved densification. In contrast, the K15 sample (Fig. 2(c3)) shows relatively loose microstructure characteristics at this temperature. This phenomenon also exists in the ceramic cores with the addition of mullite (Fig. 2(b3)), indicating that the incorporation of kyanite/mullite inhibits the densification of the ceramic cores.

Figures 3(a) and 3(b) present the XRD patterns of VPP 3D-printed ceramic cores with varying kyanite contents and sintering temperatures. The results show that the main crystal phases of the ceramic cores were cristobalite, kyanite, mullite, and zirconium silicate, as well as amorphous fused silica. Furthermore, thermodynamic and kinetic analyses demonstrate that kyanite undergoes varying degrees of decomposition within the temperature range of 1150–1250 °C, with details provided Note S3 in the ESM. This theoretical calculation is also corroborated by Fig. S2 in the ESM, which verifies that pure kyanite exhibits different extents of decomposition under these varying sintering temperatures. Additionally, magnesium oxide (MgO) was incorporated as an internal standard for quantitative analysis, with its characteristic peak observed at $2\theta \approx 42°$. MgO was selected as the internal standard because its characteristic peaks do not overlap with the characteristic peaks of the main crystal phases of the ceramic cores, facilitating the accurate correction of amorphous background interference during quantitative calculations. As shown in Fig. 3(a), no distinct cristobalite peak was observed in the C0 sample sintered at 1225 °C. However, the cristobalite peak intensity gradually increased with increasing kyanite/mullite content, suggesting that the addition of kyanite and mullite could promote the crystallization of fused silica into cristobalite. Quantitative analysis via the XRD internal standard method (Fig. 3(c)) further elucidates this behavior. At the 1225 °C sintering temperature, the cristobalite mass fraction rose from 0 to 24.42 wt% as the kyanite content increased from 0 to 20 wt%. Similarly, increasing the mullite content to 20 wt% could also raise

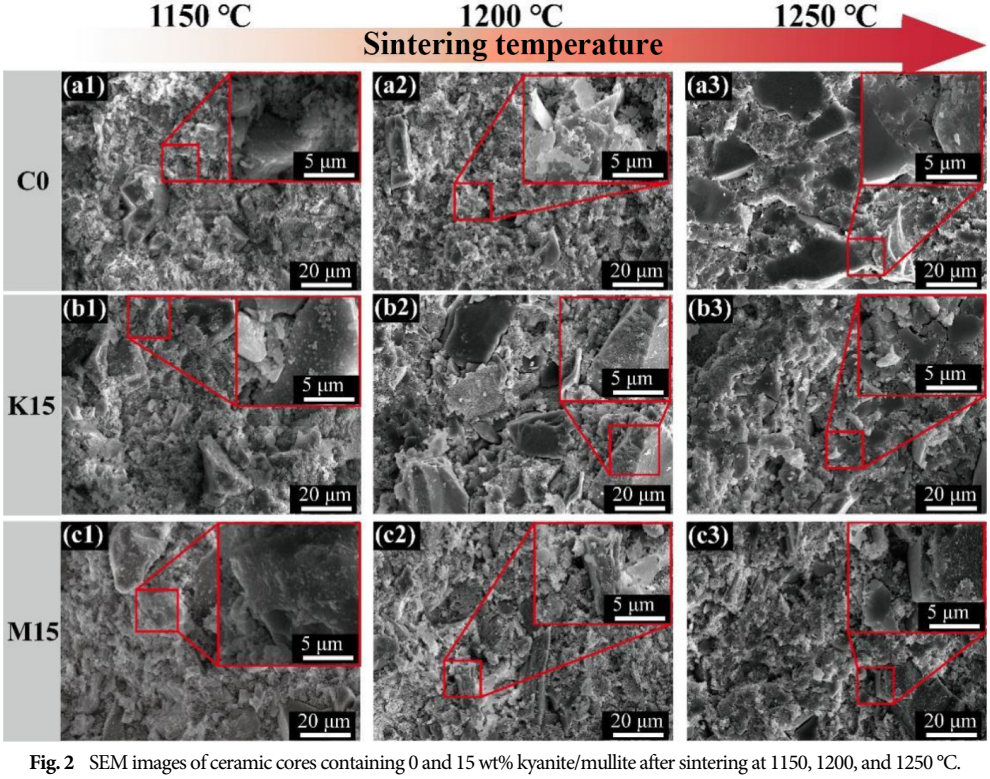

Fig. 2 SEM images of ceramic cores containing 0 and 15 wt% kyanite/mullite after sintering at 1150, 1200, and 1250 °C.

the cristobalite fraction to 29.22 wt%. These results confirm that both kyanite and mullite could promote the fused silica-to-cristobalite transformation regardless of the sintering temperature.

Notably, at a sintering temperature of 1225 °C with 15 wt% addition, the cristobalite content in the ceramic core with kyanite was 21.37 wt%, compared to 27.72 wt% in the ceramic core with mullite. This discrepancy is attributed to the difference in Al_2O_3 content. Kyanite (63.1%) contains less alumina than mullite (71.8%). Relevant studies have confirmed that kyanite and mullite can dissolve in amorphous silica particles [45]. This dissolution increases the concentration of nonbridging oxygen atoms and enhances the diffusion rate of SiO_4 tetrahedra, jointly accelerating the transformation of amorphous silica into cristobalite. Moreover, the higher the Al_2O_3 content in the mineralizer is, the more significant the promoting effect on crystallization [46]. Therefore, mullite with a higher Al_2O_3 content shows a stronger ability to promote crystallization. However, as the sintering temperature reaches 1250 °C, the final cristobalite content in the kyanite samples converges with that of the mullite samples. This is primarily due to the decomposition of kyanite at this temperature, which releases SiO_2 that rapidly transforms into cristobalite.

3.2 Thermal expansion behavior and high-temperature deflection

The modulation of ceramic powder composition and sintering temperature exerts a significant synergistic effect on the thermal expansion behavior and high-temperature deflection of VPP 3D-printed silica-based ceramic cores. Consequently, it is imperative to conduct an in-depth analysis of the underlying mechanisms governing the impact of compositional design and sintering temperature on the thermal performance of ceramic cores.

Figure 4 presents the thermal expansion curves of VPP 3D-printed ceramic cores. It can be seen in Fig. 4(a) that increasing the sintering temperature could significantly reduce the high-temperature linear shrinkage of the C0 sample. The trends across Figs. 4(a)–4(e) reveal that the overall linear shrinkage progressively decreases with increasing kyanite/mullite content. Notably, samples with a higher kyanite content exhibit distinct high-temperature thermal behavior compared to the ceramic core with mullite (Figs. 4(d) and 4(e)), characterized by a more pronounced thermal expansion at elevated temperatures. In Note S4 in the ESM, the thermal expansion trends in Figs. 4(b)–4(d) are explained. To quantify this evolution, the expansion process was divided into seven characteristic stages (Table 2). Thermal deformation (ΔK_i (DL/L values were derived from the thermal expansion curves measured in Fig. 4)) for each interval was calculated and plotted in Fig. 5.

Stage ΔT_1 corresponds to the interval where the testing temperature increases from room temperature to 220 °C. As shown in Fig. 5(a), when the sintering temperature was 1150 °C,

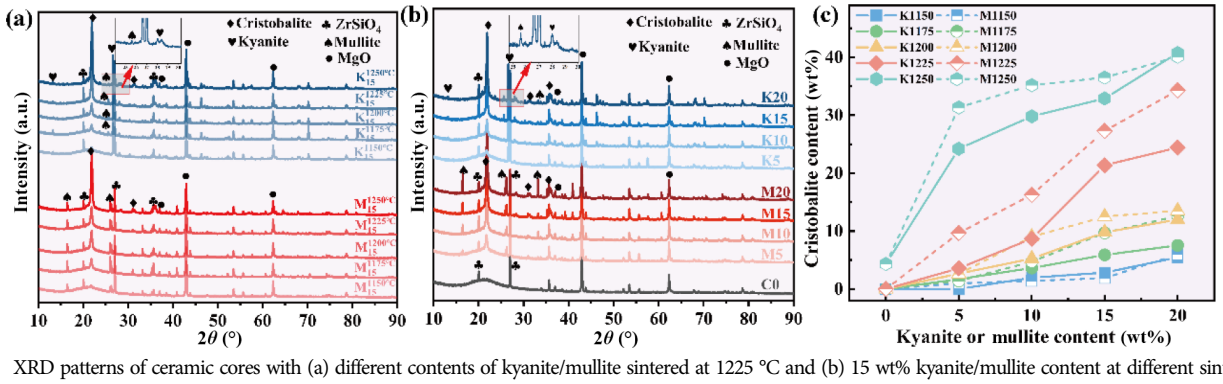

Fig. 3 XRD patterns of ceramic cores with (a) different contents of kyanite/mullite sintered at 1225 °C and (b) 15 wt% kyanite/mullite content at different sintering temperatures. (c) Cristobalite content in silica-based ceramic cores with varying kyanite/mullite contents and sintering temperatures.

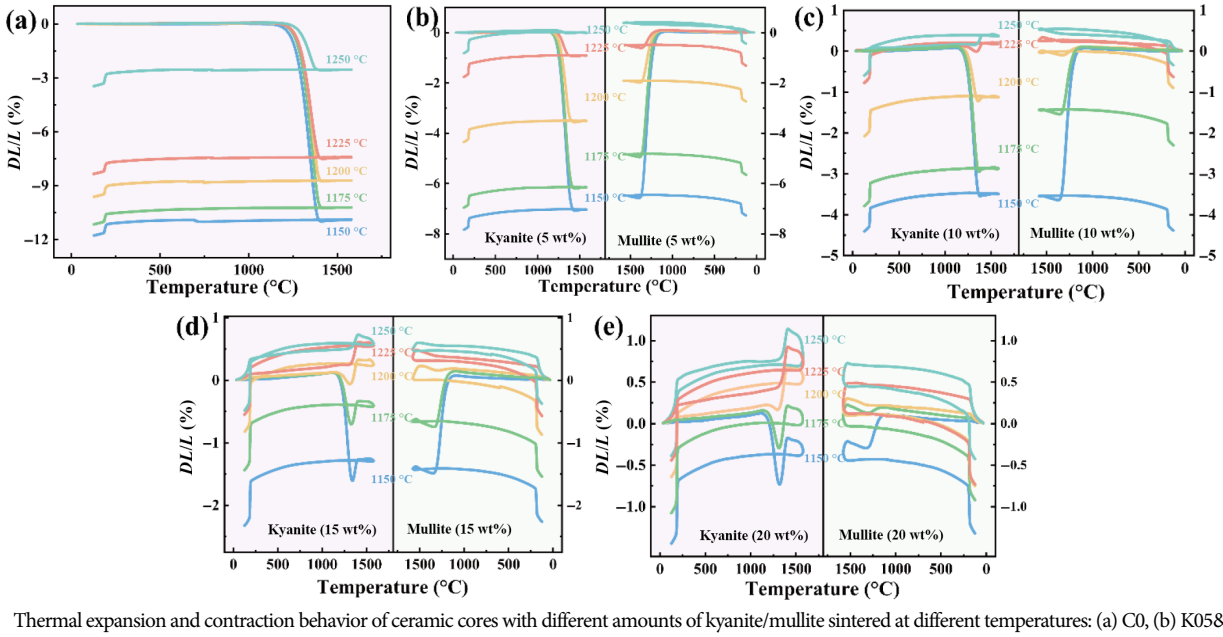

Fig. 4 Thermal expansion and contraction behavior of ceramic cores with different amounts of kyanite/mullite sintered at different temperatures: (a) C0, (b) K05&M05, (c) K10&M10, (d) K15&M15, and (e) K20&M20.

Table 2 Thermal expansion characteristic stages

Stage	No.	Temperature gradient	ΔK_i
Heating	ΔT_1	T_1(RT) – T_2(220 °C)	$\Delta K_1 = (DL/L)_{T_2} - (DL/L)_{T_1}$
	ΔT_2	T_2 (220 °C) – T_3 (1150 °C)	$\Delta K_2 = (DL/L)_{T_3} - (DL/L)_{T_2}$
	ΔT_3	T_3 (1150 °C) – T_4 (1300 °C)	$\Delta K_3 = (DL/L)_{T_4} - (DL/L)_{T_3}$
	ΔT_4	T_4 (1300 °C) – T_5 (1400 °C)	$\Delta K_4 = (DL/L)_{T_5} - (DL/L)_{T_4}$
	ΔT_5	T_5 (1400 °C) – T_6 (1580 °C)	$\Delta K_5 = (DL/L)_{T_6} - (DL/L)_{T_5}$
Cooling	ΔT_6	T_6 (1580 °C) – T_7 (220 °C)	$\Delta K_6 = (DL/L)_{T_7} - (DL/L)_{T_6}$
	ΔT_7	T_7 (220 °C) – T_8 (150 °C)	$\Delta K_7 = (DL/L)_{T_8} - (DL/L)_{T_7}$

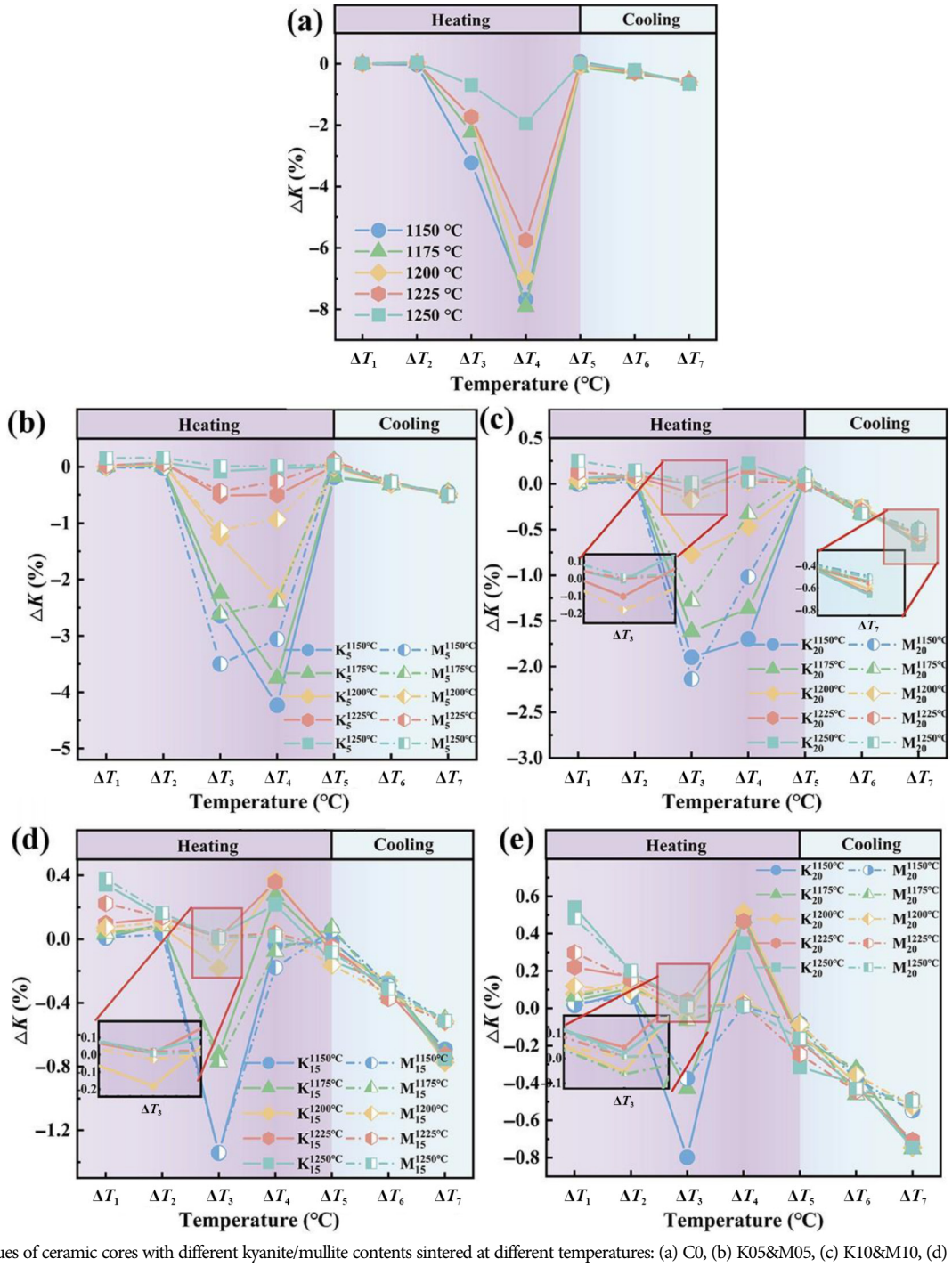

Fig. 5 ΔK values of ceramic cores with different kyanite/mullite contents sintered at different temperatures: (a) C0, (b) K05&M05, (c) K10&M10, (d) K15&M15, and (e) K20&M20.

the ΔK_1 value for the C0 sample was −0.01%. In contrast, increasing the sintering temperature to 1250 °C resulted in a ΔK_1 value of 0.01%. This transition is primarily attributed to the formation of the cristobalite phase at higher sintering temperatures. However, as illustrated in Fig. 5(e), the sample with kyanite addition exhibited a progressive increase in the magnitude of dimensional change during this stage. For instance, the ΔK_1 value for the K15 sample after sintering at 1250 °C was as high as 0.343%. For samples with added mullite, the ΔK_1 value of the samples also increased with the amount of mullite added. Specifically, the M15 sample exhibited a value of 0.381% after sintering at 1250 °C. As evidenced by the quantitative XRD results in Section 3.1, the amount of cristobalite crystallized from fused silica is positively correlated with the added amount of kyanite or mullite. Cristobalite undergoes a rapid phase transformation within this temperature range, accompanied by a volume expansion of approximately 2.8%. Consequently, the ceramic core with the addition of kyanite or mullite shows a volume expansion during the ΔT_1 stage.

Upon further heating to 1150 °C (stage ΔT_2), as illustrated in Figs. 5(a)–5(e), the thermal expansion curves of all samples displayed a steady, gradual increase without significant fluctuations. This moderate expansion is primarily attributed to intrinsic lattice vibrations within the material of ceramic cores. The testing temperature was further heated to 1300 °C (stage ΔT_3). As illustrated in Fig. 5, an increase in kyanite content within the samples leads to varying degrees of sintering shrinkage at this stage. As shown in Fig. 5(a), at a sintering temperature of 1150 °C, the ΔK_3 value for the C0 sample reached −3.23%, corresponding to the most significant shrinkage. However, when the sintering temperature was raised to 1250 °C, the ΔK_3 of the C0 sample decreased to −0.69%. A high sintering temperature could result in a high cristobalite content, which could inhibit the viscous flow of the fused silica, thereby significantly inhibiting densification. Compared with the data of Figs. 5(b)–5(d), the ΔK_3 value at stage ΔT_3 decreased progressively with increasing amounts of kyanite added. This is primarily attributed to the fact that kyanite acts as a stable high-temperature structural framework within the ceramic core, thereby suppressing viscous flow fused silica and inhibiting the secondary sintering shrinkage.

As the testing temperature rises from 1300 to 1400 °C (stage ΔT_4), silica-based ceramic cores with varying amounts of kyanite and mullite addition exhibit distinct dimensional stability. As illustrated in Fig. 5(a), the ΔK_4 of the C0 sample after sintering at 1150 °C was −4.98 %, and this value decreased to −1.27 % when the sintering temperature increased to 1250 °C. This is also attributed to the fact that the increase in sintering temperature led to an increase in cristobalite content and consequently significantly reduced the sintering shrinkage at this stage ΔT_4. As shown in Fig. 5(b), when the addition amount of kyanite increases to 5 wt%, the K5 sample sintered at 1250 °C had a ΔK_4 value decrease to −0.029%. It should be mentioned that when the addition amount of kyanite increases to 15 wt%, the corresponding ΔK_4 value reaches 0.21% rather than below zero. This indicates that the sample experienced dimensional expansion at stage ΔT_4. Guo *et al.* [41] demonstrated that kyanite undergoes thermal decomposition to form mullite and silica, accompanied by a volumetric expansion of approximately 16%–18%. This expansion counteracts the shrinkage caused by sintering densification, resulting in the expansion of the ceramic core and enhancing its thermal stability. In contrast, for ceramic cores with the addition of mullite, the ΔK_4 values of all samples in stage ΔT_4 are still less than 0 because mullite lacks volumetric expansion as kyanite does.

Subsequently, during the stage ΔT_5 (1400–1580 °C), the samples exhibited negligible dimensional changes (Fig. 5). Upon cooling to approximately 220 °C (stage ΔT_6), all ceramic core samples exhibited slight shrinkage. Finally, as the temperature dropped to 100 °C (stage ΔT_7), all ceramic cores exhibited significant volumetric shrinkage. This is driven by the transformation of cristobalite from the high-temperature phase to the low-temperature phase.

To further evaluate the high-temperature deformation resistance of ceramic cores, a high-temperature *in situ* optical observation technique was used to study the deflection at RT-1540 °C. Figure 6 presents *in situ* images illustrating the evolution of high-temperature deflection in VPP 3D-printed silica-based ceramic cores with varying amounts of kyanite/mullite after sintering at different temperatures. Based on these experimental observations, high-temperature deflection under self-weight was quantified using a double-support method at the testing temperature of 1540 °C (Fig. 7).

As shown in Figs. 6(I)(a1)–6(I)(a4), when the sintering temperature is 1150 °C, the high-temperature deflection of the C0 sample at the testing temperature of 1540 °C exceeded the measurable range. As illustrated in Figs. 6(I)(a1)–6(I)(a4) and 7, when the sintering temperature is further increased to 1250 °C, the deflection of the C0 sample at the testing temperature of 1540 °C decreases to 6.09 mm. This improvement in deflection resistance is primarily attributed to the formation of the cristobalite phase at 1250 °C. The cristobalite phase can effectively suppress the viscous flow of amorphous silica, thereby substantially enhancing the core's resistance to high-temperature deformation.

However, as shown in Fig. 7, the high-temperature deflection at the testing temperature of 1540 °C decreased progressively with increasing kyanite content. At a sintering temperature of 1250 °C, the sample with 10 wt% kyanite exhibited a significantly reduced high-temperature deflection of 2.56 mm compared to the C0 sample. Increasing the kyanite content to 20 wt% further suppressed the deflection to a mere 0.62 mm. The decrease in deflection can be primarily attributed to the formation of mullite from the thermal decomposition of kyanite, which effectively suppressed the liquid-phase flow of amorphous silica and thereby enhanced the high-temperature structural stability of the core.

In summary, increasing both the sintering temperature and kyanite content could significantly improve the high-temperature dimensional stability and the resistance to high-temperature deformation of ceramic cores. Specifically, as analyzed in Fig. 7, higher sintering temperatures promote the crystallization of cristobalite. Simultaneously, the kyanite component decomposes into mullite and silica in the ΔT_4 temperature range, resulting in a volumetric expansion. These mechanisms not only effectively mitigate thermal shrinkage through volume compensation but also generate high-temperature stable phases that inhibit the viscous flow of the amorphous silica matrix, thereby minimizing both dimensional shrinkage and deflection.

3.3 Performance analysis

For VPP 3D printing ceramic cores, the ceramic slurry mainly consists of photosensitive resin and ceramic powder. During the debinding and sintering process, the photosensitive resin in the green body thermally decomposes and volatilizes to form pores at high temperature. Existing studies confirm that changing the sintering temperature and modifying the ceramic powder composition directly govern the key properties of ceramic cores, including density, porosity, and mechanical strength. Therefore,

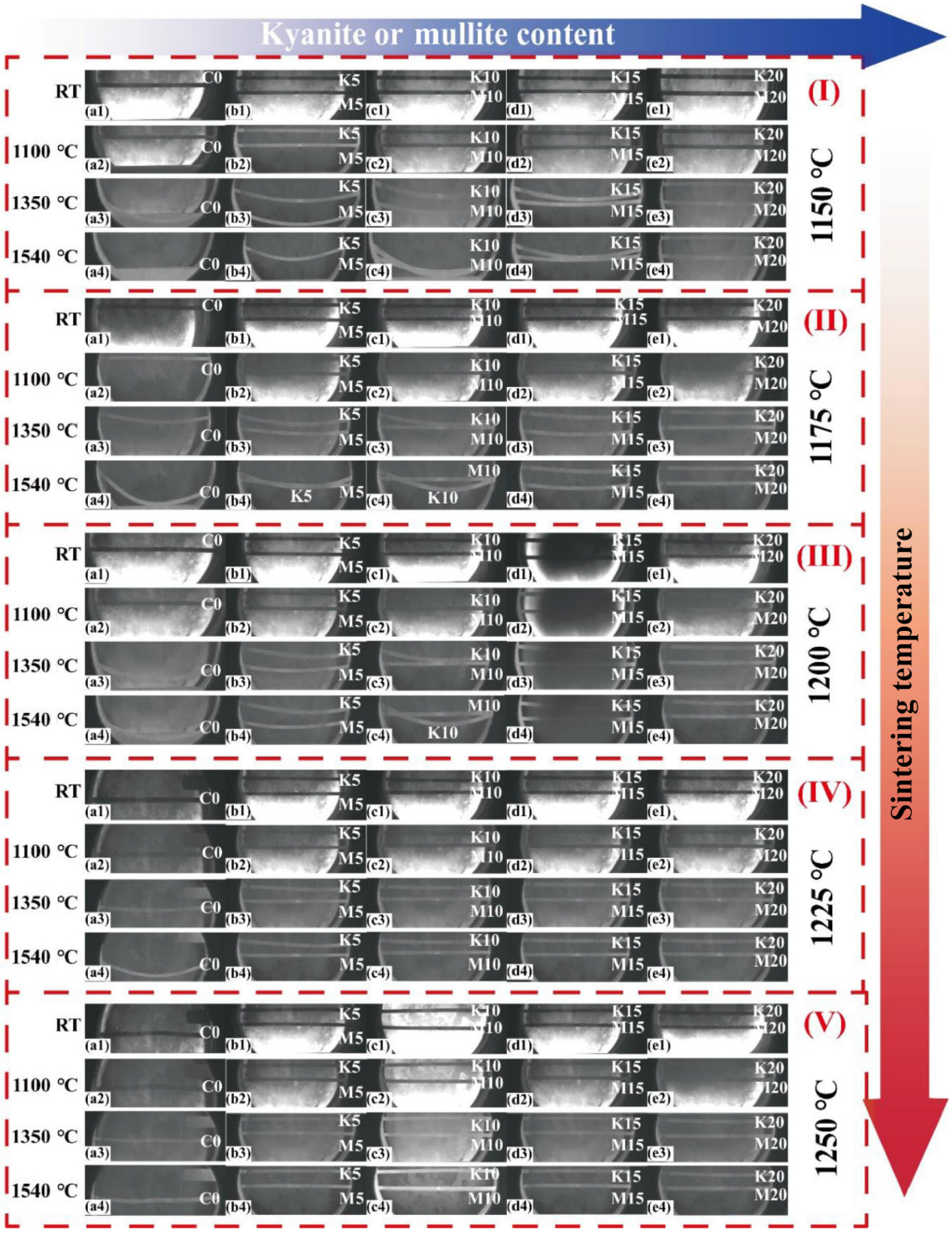

Fig. 6 *In situ* observation of high-temperature deflection for ceramic cores after sintering at 1150–1250 °C.

this section systematically studies the combined influence of varying sintering temperatures and kyanite content on the physical properties and high-temperature properties of ceramic cores.

As shown in Fig. 8, the properties of ceramic cores after sintering, specifically dimensional shrinkage, porosity, and flexural strength, are highly interconnected and fundamentally governed by sintering densification and kyanite decomposition. Generally, increasing the sintering temperature significantly promotes the densification of the ceramic cores. For instance, increasing the sintering temperature from 1150 to 1250 °C causes the sintering shrinkage of the C0 sample to surge from 1.31% to 8.25%. This is accompanied by a dramatic reduction in porosity from 29.7% to 11.25%, which consequently enhances the flexural strength from 2.6 to 14.6 MPa. Notably, the flexural strength exhibits a distinct peak at 1225 °C. This maximum strength is primarily attributed to the precipitation of an appropriate amount of cristobalite at this specific temperature, which provides stable structural reinforcement within the ceramic core [46]. However, introducing 20 wt% kyanite counteracts this densification by inhibiting the viscous flow of the silica liquid phase and generating a compensating volumetric expansion via partial decomposition of

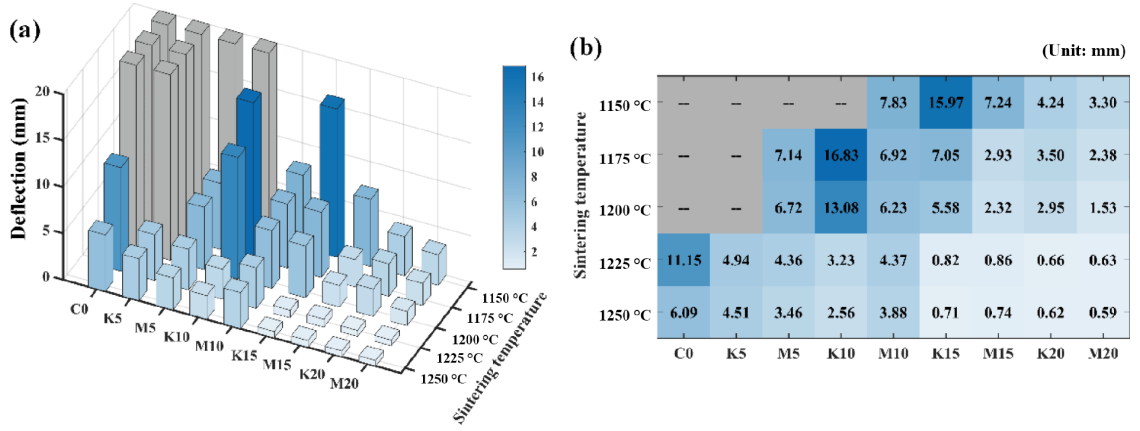

Fig. 7 High-temperature deflection at a testing temperature of 1540 °C: (a) 3D bar chart illustrating overall trend of deflection; (b) 2D heatmap showing specific deflection values.

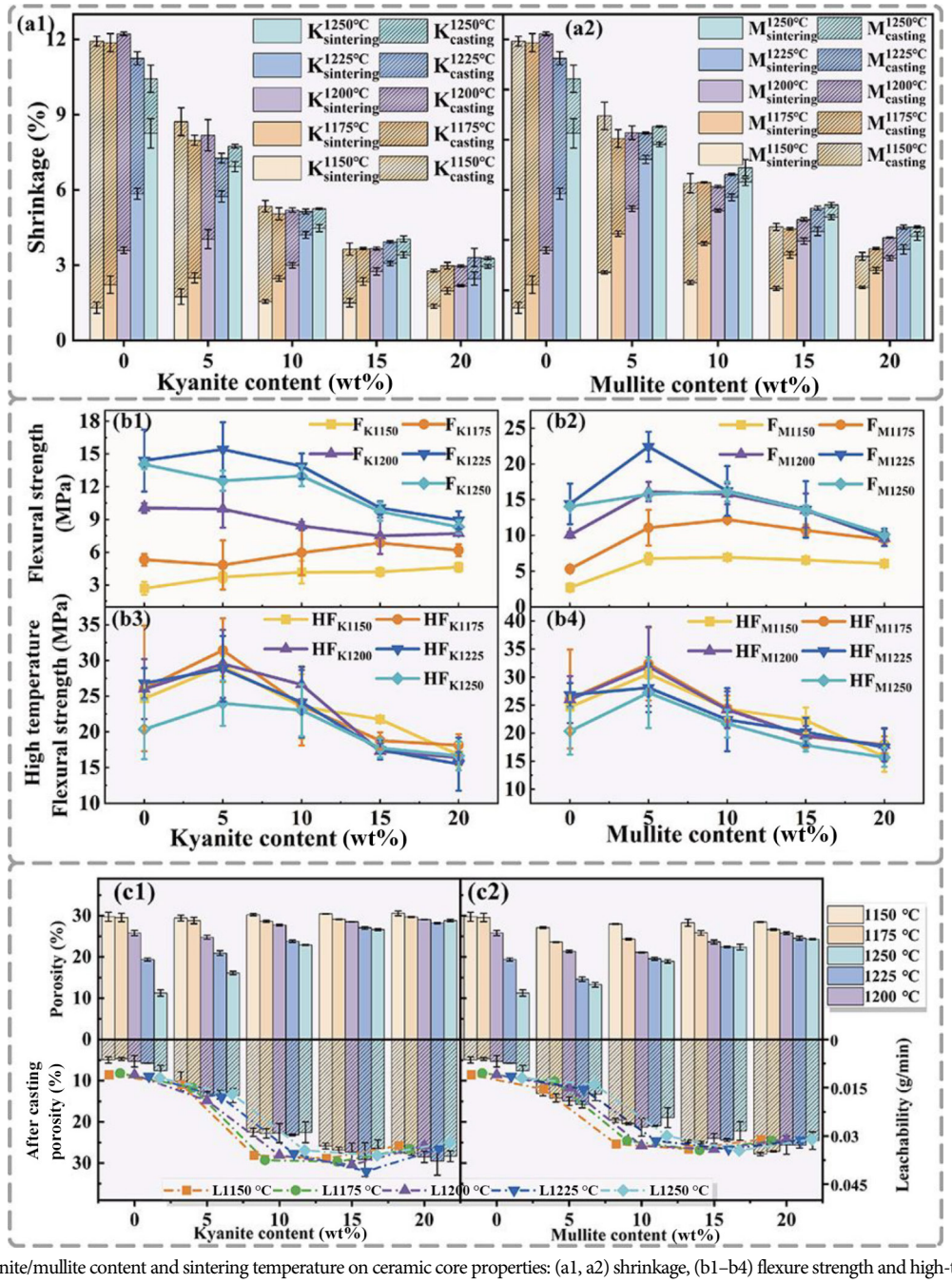

Fig. 8 Effect of kyanite/mullite content and sintering temperature on ceramic core properties: (a1, a2) shrinkage, (b1–b4) flexure strength and high-temperature flexure, and (c1, c2) porosity, porosity after casting and leachability.

the kyanite. Consequently, when sintered at 1250 °C, the sintering shrinkage is restricted to 2.94%, while the porosity increases to 28.83%. This introduces an inevitable trade-off: The increased porosity and cooling-induced microcracks from excessive cristobalite disrupt the structural continuity, decreasing the flexural strength to 8.95 MPa.

Similarly, during the simulated casting stage, the sintering temperature and kyanite content synergistically dictate the high-temperature dimensional stability, porosity after casting, and high-temperature flexural strength. Because a higher sintering temperature promotes a higher degree of crystallization and densification prior to casting [47], the casting shrinkage of the C0 sample is effectively reduced from 10.62% (sintered at 1150 °C) to 2.17% (sintered at 1250 °C). At the simulated casting temperature, the generated mullite from kyanite decomposition significantly suppresses viscous flow. Consequently, when sintered at 1250 °C, the casting shrinkage for the K20 sample is remarkably minimized to a near-zero level of 0.32%, while the porosity after casting is stably preserved at 28.33%, maintaining the internal pores essential for subsequent chemical leaching. The leaching rate initially increases and peaks at 15 wt% kyanite, primarily driven by the enhanced postcasting porosity that creates effective capillary channels for alkaline solution penetration. However, the leachability subsequently declines at higher kyanite contents. This reduction occurs because the porosity stabilizes with minimal variation, while the excessive kyanite decomposes into an increased amount of mullite. As mullite is highly insoluble in alkaline solutions, its presence ultimately acts as a barrier, restricting further dissolution of the ceramic core. In terms of the mechanical performance, for the samples sintered at 1250 °C, the high-temperature flexural strength reaches a peak of 24.05 MPa with the K5 sample but deteriorates significantly to 15.5 MPa with the K20 sample. At high temperatures, the surface of fused silica grains tends to spontaneously precipitate stable cristobalite crystals [48,49], effectively reinforcing the high-temperature strength of the ceramic cores. However, the thermal decomposition of the excessive kyanite content introduces increased porosity. Simultaneously, the significant volumetric expansion associated with the excessive cristobalite phase transformation generates extensive microcracks. The combination of these microcracks and decomposition-induced pores disrupts the structural continuity and significantly deteriorates the high-temperature mechanical performance.

In summary, the comprehensive performance of silica-based ceramic cores is significantly governed by the synergistic modulation of sintering temperature and kyanite content. Specifically, the thermal decomposition of kyanite into mullite generates a volumetric expansion. This expansion effectively counteracts sintering-induced shrinkage, ensuring superior high-temperature dimensional stability. Furthermore, the decomposition process increases the open porosity, which is beneficial for leachability. Regarding mechanical performance, moderate kyanite addition content enhances strength via skeletal reinforcement. However, excessive kyanite content compromises structural integrity due to the formation of microcracks and excessive porosity. Therefore, precise optimization of both sintering temperature and kyanite content is essential to achieve an ideal balance between dimensional accuracy and mechanical strength.

3.4 Phase evolution and thermal stability mechanisms

To elucidate the shrinkage mechanism of ceramic cores during the simulated casting process, the phase and microstructural evolutions are systematically presented in Fig. 9. The XRD results in Fig. 9(a) reveal extensive crystallization of amorphous silica into cristobalite, while the initially added kyanite undergoes complete thermal decomposition into mullite and silica. These phase transformations profoundly dictate the high-temperature microstructure. For instance, the microstructural observation in Fig. 9(b) demonstrates that without kyanite, the C0 sample generates a liquid phase that induces severe interparticle densification and macroscopic volumetric shrinkage. In contrast, Fig. 9(c2) illustrates the development of distinct high-aspect-ratio columnar grains in the K20 sample. Furthermore, the energy

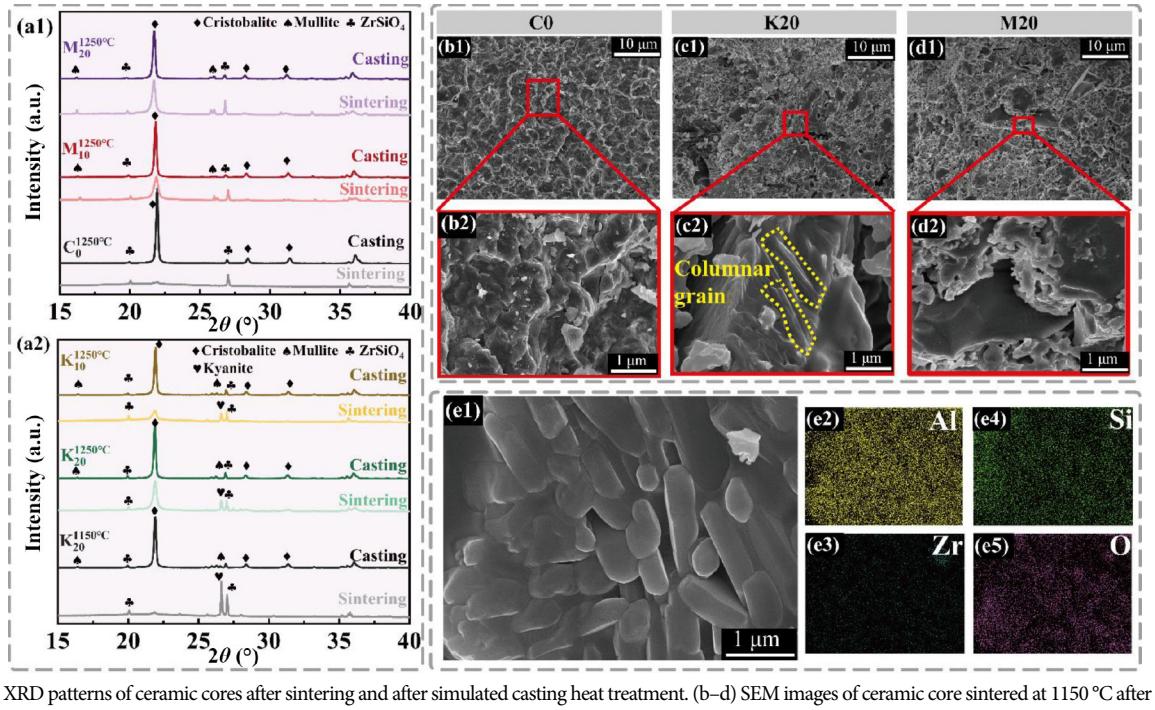

Fig. 9 (a) XRD patterns of ceramic cores after sintering and after simulated casting heat treatment. (b–d) SEM images of ceramic core sintered at 1150 °C after simulated casting heat treatment. (e) EDS analysis of columnar grains.

dispersive X-ray spectroscopy (EDS) mapping in Fig. 9(e) conclusively identifies these structures as the mullite phase, as evidenced by the exact spatial co-distribution of O, Al, and Si. Driven by preferential growth along the [001] crystallographic direction [50], the *in situ* generation of this columnar mullite plays a dual protective role: its formation provides a compensating volumetric expansion, while the thermally stable columnar skeleton robustly suppresses the viscous flow of the silica matrix. Notably, the morphology presented in Fig. 9(d) reveals that directly adding mullite (M20) fails to develop this columnar structure, underscoring that the exceptional high-temperature dimensional stability of the ceramic cores relies specifically on the *in situ* decomposition of kyanite.

As illustrated in Fig. 10(a), during the debinding stage, the resin

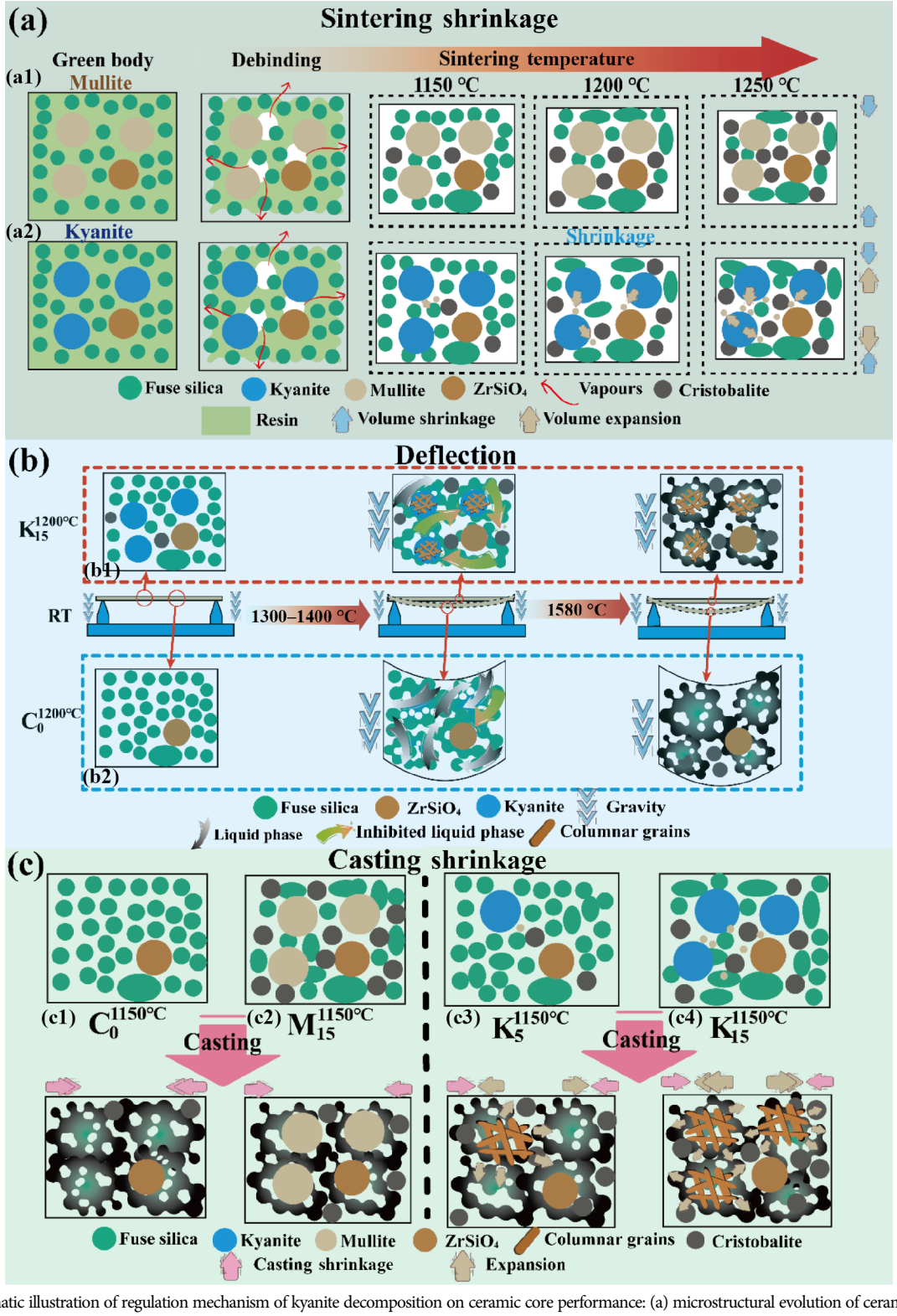

Fig. 10 Schematic illustration of regulation mechanism of kyanite decomposition on ceramic core performance: (a) microstructural evolution of ceramic cores before and after sintering, (b) high-temperature deflection of ceramic cores during casting, and (c) microstructural evolution during casting.

within the green body undergoes thermal decomposition and volatilization. As depicted by the red arrows in the debinding process, the removal of the resin results in a significant volumetric shrinkage. For samples with the addition of mullite, the mullite particles act as a thermally stable phase, effectively inhibiting the volumetric shrinkage of the ceramic core during the sintering process. In contrast, for the sample with the addition of kyanite, the kyanite particles (Fig. 10(a2)) undergo a thermal decomposition reaction during the sintering process. Based on the differential scanning calorimetry (DSC) analysis, as well as the thermodynamic and kinetic evaluations presented in Note S3 in the ESM, we elucidated the relationship between kyanite particle size and decomposition temperature. This decomposition process is accompanied by a significant volumetric expansion effect (indicated by the outward arrows), which decreases the sintering shrinkage of the ceramic core. As a result, the ceramic cores with the addition of kyanite demonstrate a significantly smaller sintering shrinkage than those with the addition of mullite. Figure 10(b) schematically illustrates the high-temperature deflection mechanisms of the ceramic cores during the casting process, contrasting the distinct behaviors of the C0 and K15 samples sintered at 1200 °C. For the C0 sample (Fig. 10(b2)), the microstructure in the temperature range of 1300–1400 °C is predominantly composed of amorphous silica with dispersed zirconium silicate particles. Due to the lack of high-temperature stable phases, the ceramic core begins to soften and deform within the range of 1300–1400 °C, with deformation persisting at 1540 °C. In contrast, for the K15 sample, kyanite transforms into columnar mullite crystals at 1400 °C. The mullite produced by the decomposition of kyanite serves as a high-temperature stable phase to effectively minimize deformation and significantly enhance the ceramic core's high-temperature stability.

Figure 10(c) schematically illustrates the microstructural evolution during the simulated casting process. As shown in Fig. 10(c1), for the C0 sample, due to the absence of high-temperature stable phases, the ceramic core exhibits a high degree of sintering densification, which in turn leads to significant shrinkage. In the case of the M15 sample, the shrinkage is noticeably reduced. This is because the mullite particles formed a skeleton network within the ceramic core and effectively inhibited the densification of the surrounding fused silica due to their high thermal stability. As shown in Figs. 10(c3) and 10(c4), the kyanite particles transform into columnar mullite crystals, accompanied by a volumetric expansion represented by the yellow arrows. In Note S3 in the ESM, it is demonstrated that at the casting temperature, the large-grained kyanite begins to decompose into mullite. This expansion effectively counteracts the casting shrinkage (pink arrows). Comparing the microstructure of K5 with K15 reveals that increasing the kyanite content generates more columnar mullite crystals, thereby achieving more effective compensation for casting shrinkage and superior high-temperature dimensional stability.

3.5 Comprehensive performance evaluation of ceramic cores

To meet the stringent requirements of investment casting for aeroengine hollow turbine blades, silica-based ceramic cores must satisfy a series of mutually constraining and multidimensional performance criteria. This study systematically investigated the effects of kyanite content and sintering temperature on sintering shrinkage after casting shrinkage, high-temperature creep resistance, mechanical strength, and microstructural evolution. However, significant trade-offs often exist among these performance indicators. For instance, although increasing the kyanite content can effectively suppress sintering shrinkage, it often compromises the mechanical strength. Similarly, raising the sintering temperature can improve flexure strength but leads to a significant reduction in porosity and excessive shrinkage. To systematically evaluate the performance of VPP 3D-printed ceramic cores, a "CQI" evaluation model was established. By employing dimensionless normalization and weighted integration of eight performance parameters, this model facilitates integrated characterization and simplifies the analysis of complex multivariate data. Given the significant disparities in physical units and orders of magnitude among the parameters, dimensionless normalization was performed on the raw data to eliminate dimensional bias. Furthermore, based on multiobjective optimization criteria, the indicators were categorized into "Higher-the-Better" and "Lower-the-Better" classes [51], signifying that superior performance is defined by larger and smaller values, respectively. The specific definitions of these indicators are detailed in Table 3.

Figure 11(a1) presents the radar charts illustrating the distribution of performance data for ceramic cores with different formulations at the same sintering temperature. Due to significant disparities in units and orders of magnitude among various physical properties, achieving an objective comprehensive evaluation is challenging. To eliminate these influences, Fig. 11(a2) shows the data onto a dimensionless interval via normalization, thereby placing all performance metrics within an equivalent evaluation way. In this way, the size of the radar chart's enclosed area reflects the quality of the comprehensive performance. A larger polygon signifies an optimal balance of mechanical strength, thermal stability, and shrinkage. This transformation not only enhances the intuitiveness of the evaluation but also provides direct support for the subsequent quantitative analysis of CQIs.

The ceramic CQI of ceramic cores is as shown in the Eq. (1):

Table 3 Definitions, optimization characteristics, and normalization formulas of performance evaluation indicators for silica-based ceramic cores

Performance evaluation index	Performance	Normalization formula
Performance lower-the-better index	Sintering shrinkage, x_1 Casting shrinkage, x_2 $\sum_{i=1}^{5} \Delta K_i$, x_3 Deflection, x_4	$N_j = \left(x_{j,\max} - x_j\right) / \left(x_{j,\max} - x_{j,\min}\right)$ (j = 1–4)
Performance higher-the-better index	Porosity, x_5 Leachability, x_6 Flexure strength, x_7 High-temperature flexure strength, x_8	$N_k = \left(x_k - x_{k,\min}\right) / \left(x_{k,\max} - x_{k,\min}\right)$ (k = 5–8)

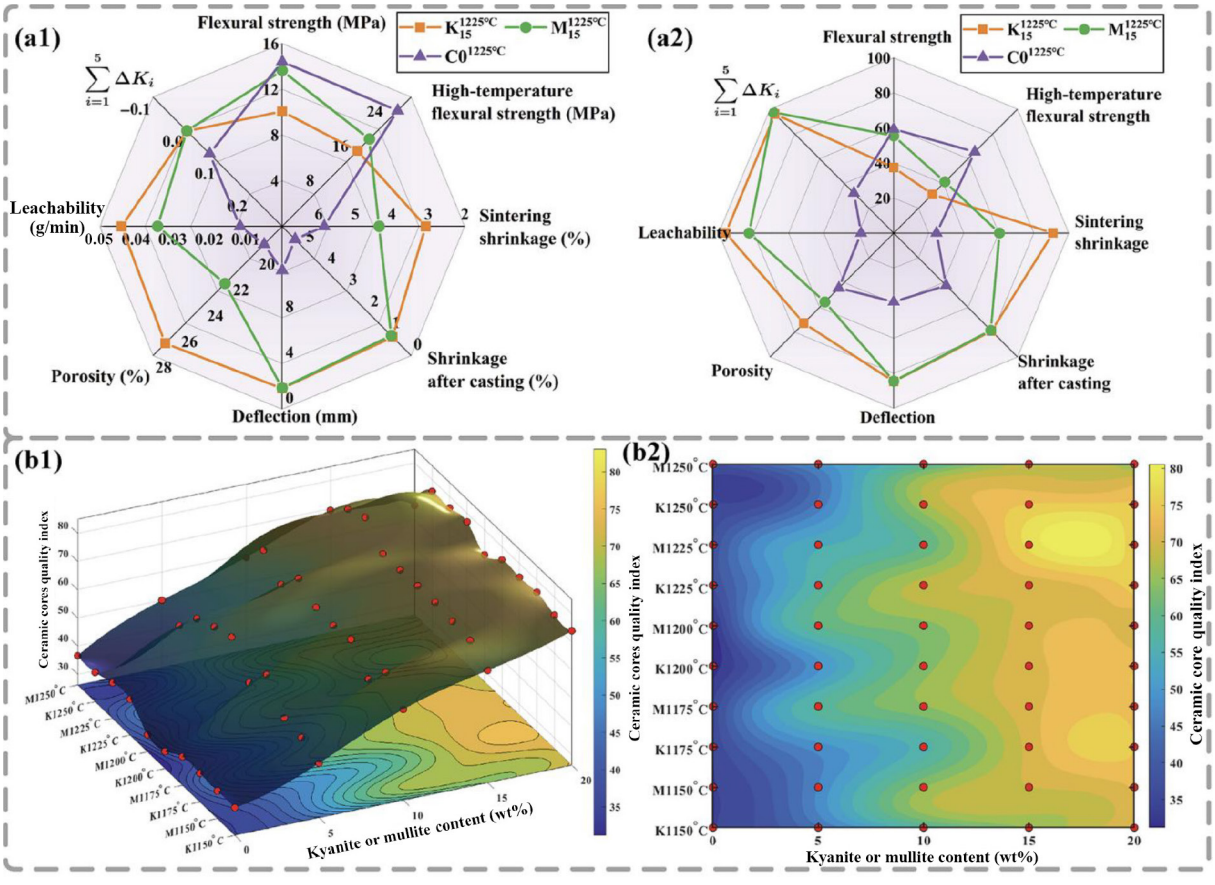

Fig. 11 Comparative analysis of multidimensional performance of ceramic cores: (a1) radar chart displaying multidimensional raw performance data of ceramic cores; (a2) radar chart of normalized performance evaluation metrics; (b1) response surface plot illustrating interaction effects of kyanite content and sintering temperature on CQI; (b2) corresponding 2D contour projection of response surface.

$$\mathrm{CQI} = \sum_{i=1}^{8} (\omega_i N_i) \times 100 \tag{1}$$

where ω_i represents the weight of the i indicator ($\sum \omega_i = 1$) and N_i denotes the normalized value of each performance indicator. A higher CQI value indicates a better synergistic balance between mechanical properties and shrinkage. This model intuitively and quantitatively characterizes how kyanite content and sintering temperature regulate the comprehensive performance of the cores. The assignment of weights fully balances the varying constraints during different service stages, such as wax injection, ceramic shell manufacturing and casting. Notably, sintering shrinkage ($\omega = 0.25$) and shrinkage after casting ($\omega = 0.15$) account for the highest weights. The dimensional changes during sintering and casting directly determine the consistency of the hollow blade wall thickness and the acceptance rate. Meanwhile, high-temperature deflection ($\omega = 0.15$) and the cumulative thermal deformation ($\omega = 0.05$) across different temperature ranges (ΔT_1–ΔT_5) constitute the thermal stability score. This objectively reflects the geometric fidelity of the core in extreme environments above 1500 °C. The flexure strength ($\omega = 0.10$) and high-temperature flexure strength ($\omega = 0.10$) ensure the yield during wax injection and the structural integrity during casting, respectively. Furthermore, residual pores after casting serve as critical physical channels for chemical leaching. Since their contribution to reducing the scrap rate is more decisive, this study assigns a higher weight to leachability ($\omega = 0.15$) than to sintering porosity ($\omega = 0.05$). The analysis related to the assignment of weights of indicators can be found in Note S5 in the ESM.

Based on the constructed CQI mathematical model, the response surface and its contour projection were plotted (Fig. 11(b)). These plots illustrate how the CQI evolves with the kyanite content and sintering temperature. As shown in Fig. 11(b1), the CQI initially increases and then decreases with increasing kyanite content and sintering temperature. Through the projection analysis in Fig. 11(b2), the optimal processing window for high-performance cores can be clearly defined. Experimental results indicate that the CQI reaches its global maximum (CQI = 78.85) at a sintering temperature of 1225 °C and kyanite content of 15 wt%. Under these conditions, the addition of kyanite effectively offsets the viscous flow shrinkage of the fused silica. This compensation maintains the casting shrinkage at a very low level. Ceramic cores prepared under these conditions exhibit excellent flexure strength, high-temperature flexure strength, and low high-temperature deflection. Meanwhile, the higher porosity after casting ensures the efficiency of the subsequent chemical leaching process. In summary, the CQI model successfully simplifies the processing of multidimensional experimental data and effectively overcomes the limitations of traditional single-parameter evaluations when dealing with conflicting properties. The evaluation results confirm that this optimized process is the best solution for fabricating high-performance VPP 3D-printed ceramic cores. It fully meets the comprehensive and rigorous requirements of advanced aeroengine investment casting.

4 Conclusions

In this study, silica-based ceramic cores were fabricated via VPP 3D printing, and the effects of kyanite content and sintering

temperature on their comprehensive performance were systematically investigated. To balance the competing performance indicators, we established the ceramic CQI as a quantitative evaluation model. The optimal parameters were identified as a 15 wt% kyanite content with a 1225 °C sintering temperature. This formulation demonstrated outstanding performance, including a sintering shrinkage of 3.06%, a simulated casting shrinkage of 0.86%, room-temperature and high-temperature flexural strengths of 10.06 and 27.05 MPa, respectively, and a high-temperature deflection of 0.82 mm. Calculated through the proposed model, this optimized formulation obtained the highest global CQI score of 78.85. This work provides a reliable evaluation methodology and a novel strategy to simultaneously enhance the dimensional accuracy and high-temperature stability of 3D-printed ceramic cores.

Acknowledgements

This work was supported by the National Natural Science Foundation of China (No. 52172072).

Author contributions

Boran Wang: Writing—original draft, Methodology, Investigation, Formal analysis, Data curation. Zhongyan Wang: Writing—review and editing, Conceptualization. Xin li: Writing—review and editing, Formal analysis. Yu Chen: Writing—review and editing, Investigation. Rui Ge: Writing—review and editing, Investigation. Yongkang Yang: Writing—review and editing, Methodology. Jiachen Liu: Writing—review and editing, Funding acquisition. Anran Guo: Writing—review and editing, Funding acquisition, Formal analysis, Conceptualization.

Availability of data and materials

The data that support the findings of this study are available from the corresponding author upon reasonable request.

Competing interests

The authors have no competing interests to declare that are relevant to the content of this article.

Electronic Supplementary Material

Supplementary material is available in the online version of this article at https://doi.org/10.26599/JAC.2026.9221313.

References

[1] Liu JQ, Li QL, Huo MD, *et al.* Microstructure and mechanical properties of 3D-printed nano-silica reinforced alumina cores. *Ceram Int* 2022, **48**: 30282–30293.

[2] Gromada M, Świeca A, Kostecki M, *et al.* Ceramic cores for turbine blades via injection moulding. *J Mater Process Tech* 2015, **220**: 107–112.

[3] Pattnaik S, Karunakar DB, Jha PK. Developments in investment casting process—A review. *J Mater Process Tech* 2012, **212**: 2332–2348.

[4] Li H, Liu YS, Liu YS, *et al.* Evolution of the microstructure and mechanical properties of stereolithography formed alumina cores sintered in vacuum. *J Eur Ceram Soc* 2020, **40**: 4825–4836.

[5] Bae CJ, Kim D, Halloran JW. Mechanical and kinetic studies on the refractory fused silica of integrally cored ceramic mold fabricated by additive manufacturing. *J Eur Ceram Soc* 2019, **39**: 618–623.

[6] Pollock TM, Tin S. Nickel-based superalloys for advanced turbine engines: Chemistry, microstructure and properties. *J Propuls Power* 2006, **22**: 361–374.

[7] Zheng W, Wu JM, Chen S, *et al.* Fabrication of high-performance silica-based ceramic cores through selective laser sintering combined with vacuum infiltration. *Addit Manuf* 2021, **48**: 102396.

[8] Gu Y, Duan WY, Wang TC, *et al.* Additive manufacturing of Al_2O_3 ceramic core with applicable microstructure and mechanical properties via digital light processing of high solid loading slurry. *Ceram Int* 2023, **49**: 25216–25224.

[9] Li QL, Chen TC, Liang JJ, *et al.* Manufacturing of ceramic cores: From hot injection to 3D printing. *J Mater Sci Technol* 2023, **134**: 95–105.

[10] Yang YK, Xu XQ, Wang BR, *et al.* Optimisation of curing models and ultra-high-precision forming strategy in vat photopolymerization of silica-based ceramic modified by graphene. *Virtual Phys Prototyp* 2025, **20**: 2499450.

[11] Wang BR, Yang YK, Li X, *et al.* Enhancing forming precision and performance of silica-based ceramic cores via vat photopolymerization. *Virtual Phys Prototyp* 2025, **20**: 2565476.

[12] Cao YQ, Xu XJ, Qin Z, *et al.* Vat photopolymerization 3D printing of thermal insulating mullite fiber-based porous ceramics. *Addit Manuf* 2022, **60**: 103235.

[13] Su RY, Chen JY, Zhang XQ, *et al.* Accuracy controlling and mechanical behaviors of precursor-derived ceramic SiOC microlattices by projection micro stereolithography (PμSL) 3D printing. *J Adv Ceram* 2023, **12**: 2134–2147.

[14] Zhang XQ, Su RY, Gao X, *et al.* 3D-printed polyurea-toughened Al_2O_3 cellular ceramic structures: Bioinspired dual-phase interpenetrating design for superior mechanical properties. *J Adv Ceram* 2025, **14**: 9221095.

[15] Zhang F, Zhou SX, You HY, *et al.* 3D printing of ceramic matrix composites: Strengthening and toughening strategies. *Compos Part B-Eng* 2025, **297**: 112335.

[16] Sun J, Zhang JD, Zhang X, *et al.* High strength mullite-bond SiC porous ceramics fabricated by digital light processing. *J Adv Ceram* 2024, **13**: 53–62.

[17] Li X, Su HJ, Dong D, *et al.* Enhanced comprehensive properties of stereolithography 3D printed alumina ceramic cores with high porosities by a powder gradation design. *J Mater Sci Technol* 2022, **131**: 264–275.

[18] Zakeri S, Vippola M, Levänen E. A comprehensive review of the photopolymerization of ceramic resins used in stereolithography. *Addit Manuf* 2020, **35**: 101177.

[19] Alves MFRP, dos Santos C, Duarte I, *et al.* Complex shapes of lithium disilicate glass-ceramics developed by material extrusion. *Addit Manuf* 2024, **80**: 103973.

[20] Liu SQ, Li QL, Qu BY, *et al.* Cooperative control of sintering shrinkage and strength of stereolithography 3D printed silica-based ceramic cores. *Ceram Int* 2025, **51**: 19435–19448.

[21] Zhou SX, Liu GZ, Chen AN, *et al.* Effect of molecular weight and chemical structure of plasticizer on suspension property, binder removal, and sintered performance for zirconia toughened alumina ceramics fabricated by vat photopolymerization. *J Eur Ceram Soc* 2024, **44**: 116730.

[22] Guo YY, Zhao XN, Guan JX. Construction of hydroxyapatite bioceramics with biomimetic structures by weak magnetic field-assisted 3D printing. *J Adv Ceram* 2025, **14**: 9221144.

[23] Gu QC, Wang HL, Gao WJ, *et al.* Preparation of large-size alumina ceramic parts by DLP 3D printing using high-solid-loading paste and optimizing the debinding process. *Ceram Int* 2023, **49**: 28801–28812.

[24] Kim J, Gal CW, Choi YJ, *et al.* Effect of non-reactive diluent on defect-free debinding process of 3D printed ceramics. *Addit Manuf* 2023, **67**: 103475.

[25] Kim EH, Park HY, Lee CL, *et al.* Single crystal casting of gas turbine blades using superior ceramic core. *J Mater Res Technol* 2020, **9**: 3348–3356.

[26] Pan ZP, Guo JZ, Li SM, *et al.* Experimental study on high temperature performances of silica-based ceramic core for single crystal turbine blades. *Ceram Int* 2022, **48**: 548–555.

[27] Dong RZ, Wang WH, Cui K, *et al.* Core shifting prediction in filling

process of hollow turbine blade investment casting. *J Manuf Process* 2023, **86**: 253–265.
[28] Zhang YZ, Duan WY, Gu Y, *et al.* Manufacturing process of water-soluble salt-based ceramic cores based on vat photopolymerization. *J Adv Ceram* 2024, **13**: 652–665.
[29] Fan JX, Xu XQ, Niu SX, *et al.* Anisotropy management on microstructure and mechanical property in 3D printing of silica-based ceramic cores. *J Eur Ceram Soc* 2022, **42**: 4388–4395.
[30] Pilate P, Lardot V, Cambier F, *et al.* Contribution to the understanding of the high temperature behavior and of the compressive creep behavior of silica refractory materials. *J Eur Ceram Soc* 2015, **35**: 813–822.
[31] Pascova R, Avdeev G, Gutzow I, *et al.* Refractory alkali-free cristobalite glass-ceramics: Activated reaction sinter-crystallization synthesis and properties. *Int J Appl Glass Sci* 2012, **3**: 75–87.
[32] Breneman RC, Halloran JW. Effect of cristobalite on the strength of sintered fused silica above and below the cristobalite transformation. *J Am Ceram Soc* 2015, **98**: 1611–1617.
[33] Kim YH, Yeo JG, Lee JS, *et al.* Influence of silicon carbide as a mineralizer on mechanical and thermal properties of silica-based ceramic cores. *Ceram Int* 2016, **42**: 14738–14742.
[34] Pan ZP, Lu BP, Guo JZ, *et al.* Microstructures and properties of silica-based ceramic cores reinforced by alumina sol-modified fused-silica fibers. *Ceram Int* 2024, **50**: 10602–10608.
[35] Niu SX, Xu XQ, Li X, *et al.* Microstructure evolution and properties of silica-based ceramic cores reinforced by mullite fibers. *J Alloys Compd* 2020, **829**: 154494.
[36] Qu BY, Li QL, Liu SQ, *et al.* Controlling the cristobalite content, microstructure, and properties of vat photopolymerization 3D printed SiO_2-based ceramic cores by doping Fe_2O_3. *Ceram Int* 2025, **51**: 15535–15546.
[37] Liang JJ, Lin QH, Zhang X, *et al.* Effects of alumina on cristobalite crystallization and properties of silica-based ceramic cores. *J Mater Sci Technol* 2017, **33**: 204–209.
[38] Kim YH, Yeo JG, Choi SC. Shrinkage and flexural strength improvement of silica-based composites for ceramic cores by colloidal alumina infiltration. *Ceram Int* 2016, **42**: 8878–8883.
[39] Comodi P, Zanazzi PF, Poli S, *et al.* High-pressure behavior of kyanite; compressibility and structural deformations. *Am Mineral* 1997, **82**: 452–459.
[40] Liu Y, Xu L, Chen M, *et al.* Effects of andalusite and kyanite addition on the microstructure, thermo-mechanical properties and corrosion resistance of ultralow-cement bauxite-corundum castables. *Ceram Int* 2022, **48**: 14141–14150.
[41] Guo HS, Ye FB, Li WF, *et al.* Preparation and characterization of foamed microporous mullite ceramics based on kyanite. *Ceram Int* 2015, **41**: 14645–14651.
[42] Saruhan B, Albers W, Schneider H, *et al.* Reaction and sintering mechanisms of mullite in the systems cristobalite/α-Al_2O_3 and amorphous SiO_2/α-Al_2O_3. *J Eur Ceram Soc* 1996, **16**: 1075–1081.
[43] Barlett HB. Rate of decomposition of kyanite at various temperatures. *J Am Ceram Soc* 1940, **23**: 249–251.
[44] Qin YX, Pan W. Effect of kyanite on properties of alumina-based ceramic core composites. *Rare Met Mater Eng* 2009, **38**: 223–225.
[45] Kazemi A, Faghihi-Sani MA, Alizadeh HR. Investigation on cristobalite crystallization in silica-based ceramic cores for investment casting. *J Eur Ceram Soc* 2013, **33**: 3397–3402.
[46] Zheng W, Wu JM, Chen S, *et al.* Influence of Al_2O_3 content on mechanical properties of silica-based ceramic cores prepared by stereolithography. *J Adv Ceram* 2021, **10**: 1381–1388.
[47] Wang LY, Hon MH. The effect of cristobalite seed on the crystallization of fused silica based ceramic core—a kinetic study. *Ceram Int* 1995, **21**: 187–193.
[48] Wilson PJ, Blackburn S, Greenwood RW, *et al.* The role of zircon particle size distribution, surface area and contamination on the properties of silica–zircon ceramic materials. *J Eur Ceram Soc* 2011, **31**: 1849–1855.
[49] Kazemi A, Faghihi-Sani MA, Nayyeri MJ, *et al.* Effect of zircon content on chemical and mechanical behavior of silica-based ceramic cores. *Ceram Int* 2014, **40**: 1093–1098.
[50] Schneider H, Majdič A. Kinetics of the thermal decomposition of kyanite. *Ceram Int* 1985, **11**: 142.
[51] Chen CH. A novel multi-criteria decision-making model for building material supplier selection based on entropy-AHP weighted TOPSIS. *Entropy* 2020, **22**: 259.